Experiments in Fluids 33 (2002) 940–949
DOI 10.1007/s00348-002-0514-8

POD analysis of flow structures in a scale model of a ventilated room

J.M. Pedersen, K.E. Meyer

Abstract Measurements with particle image velocimetry have been carried out in a scale model of the Annex 20 room. Data were taken in a plane near the inlet. The flow consisted of a wall jet (Re=5,000) and a low-velocity region below the jet. POD was used to analyze dominant flow structures. The analysis showed that the flow some of the time has flow structures very different from the mean velocity field. A time-resolved data series was projected onto the orthonormal basis derived from the POD for analysis of the time variation of the POD amplitudes.

1 Introduction

The Annex 20 room (Nielsen 1990) is a standard measure room which is used for investigation of ventilation problems and indoor environment. It has been constructed such that its shape and the inlet/outlet conditions are representative of a typical room in an office building. Of special interest are human-comfort parameters such as draught (maximum local velocities) and transport of pollutants. From a fluid mechanics point-of-view the flow poses a great challenge. A turbulent wall jet is formed by the inlet. For a review of the turbulent wall jet, see George et al. (2000). The jet region is highly turbulent, while other regions of the room are characterized by very low velocities. Thus, the flow involves laminar–turbulent transition, which makes numerical investigation by turbulence modeling for the Reynolds-averaged Navier–Stokes equations (RANS) difficult, see, for example, Chen (1995). The flow evolves quite slowly in time and low sampling rates are required for the measured data to be statistically uncorrelated. Hence, measurement of mean quantities becomes very time consuming with point-wise measurement techniques like hot-wire and laser Doppler anemometry (LDA). These features suggest that great advantage may be derived from the use of particle image velocimetry (PIV) for investigation of the flow in the Annex 20 room. Mean quantities are determined at many locations simultaneously, greatly reducing the amount of time necessary compared to, for example, LDA. Having sampled appropriate data, another obvious application would be comparison with numerical data to verify results from different turbulence models or large-eddy simulation (LES).

A way to extract the dominant structures of a flow is by application of the proper orthogonal decomposition (POD) technique (Lumley 1970; Moin and Moser 1989). This technique is interesting for several reasons. It may be used to compare the instantaneous flow structures found from PIV data to results from LES. It is a powerful tool in the context of data reduction and hence may also be used to create databases with, for example, inlet conditions for use in numerical simulations. In the studies presented here, the PIV data obtained are analyzed with regard to a study of the flow structures appearing in the flow of the Annex 20 room. POD is used to find the dominant structures of the flow in the measuring domain considered. Due to the large time scales, a satisfactory time resolution of the flow may be obtained from PIV data taken at high sampling rate (10 Hz). This is utilized in the last part of the paper, where the temporal evolution of the flow is studied by projecting the temporally resolved velocity data onto the POD basis obtained from the statistical analysis.

2 Experimental setup

A Perspex 1:15-scale model of the Annex 20 room was constructed, using water as fluid, to facilitate measurements with PIV. Figure 1 shows a 2D sketch of the model. Flow chambers were placed before and after the actual Annex 20 part to ensure appropriate inlet and outlet conditions. Fluid was supplied at the upper left of the room and exited at the lower right. The dimensions of the model room are: length: L=600 mm, height: H=200 mm, width: W=200 mm, inlet height: h=11.2 mm, and outlet height: t=32 mm. The Reynolds number, $Re\approx$5,000, is based on the mean inlet velocity, $u_0\approx$0.45 m/s and the inlet height. Earlier studies, both experimental and numerical, have used Reynolds numbers of a similar magnitude (Nielsen et al. 1978; Chen 1995). For this Re value, the mean flow is characterized by a large recirculation zone (indicated by arrows in Fig. 1) in the center of the room and two small recirculation zones appearing in the corners to the lower left and the upper right. The measurements were taken in a square section in the region $0<x<200$ mm and $0<y<200$ mm at z=0, as indicated in Fig. 1 by the dashed square right after the inlet. Figure 2 shows the whole setup with placement of model, camera, and the light-sheet optics forming the laser sheet in the measuring domain. The pipes indicated at both ends of the

Accepted: 3 June 2002
Published online: 18 September 2002

J.M. Pedersen (✉), K.E. Meyer
Department of Mechanical Engineering,
Fluid Mechanics Section, Technical University of Denmark,
Building 403, 2800 Lyngby, Denmark
E-mail: jmp@mek.dtu.dk

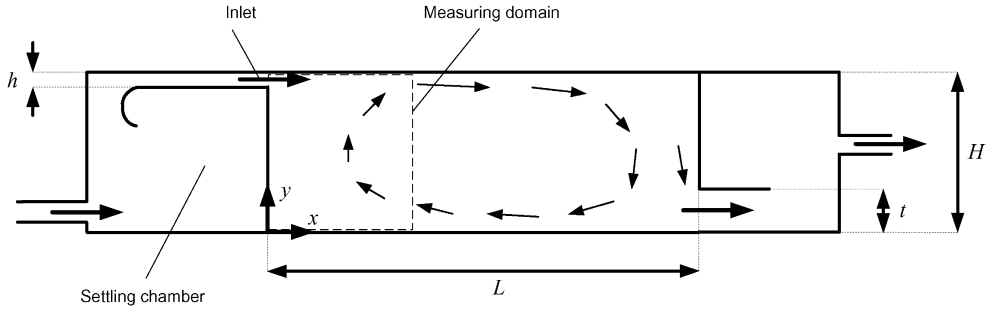

Fig. 1. A 2D sketch of the model with inlet and outlet chambers and definition of coordinate system

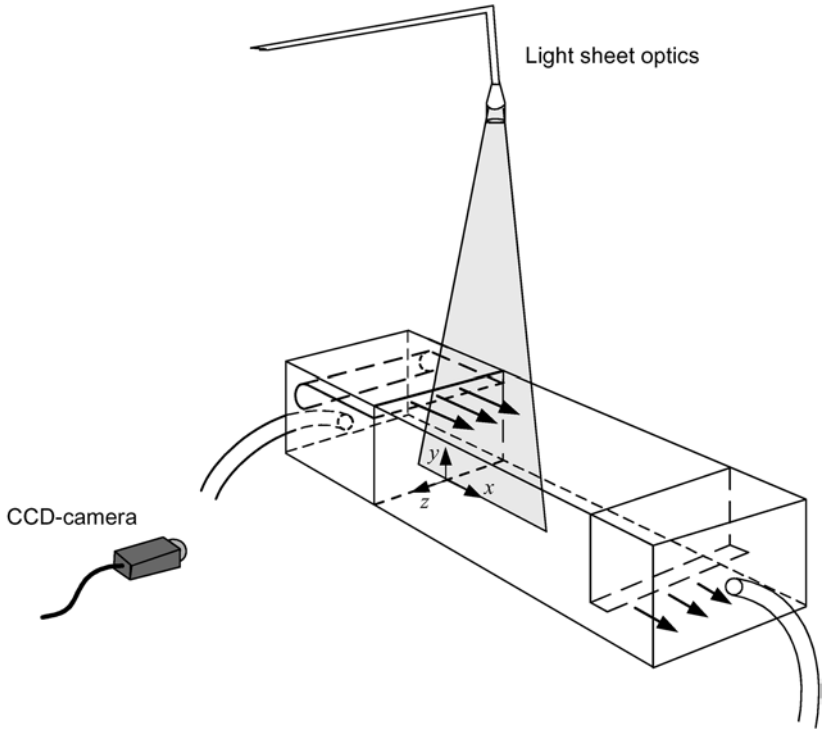

Fig. 2. Experimental setup with scale model, camera, and light-sheet optics

model were connected to a circulation unit placed below the model. The circulation unit consisted of a pump and an orifice flow meter connected to a manometer for controlling the flow rate. The flow rate was adjusted by changing the number of revolutions per minute of the pump.

The measuring equipment was a Kodak MegaPlus ES 1.0 camera and a double-cavity Nd-YAG laser delivering 100 mJ per light pulse. The data collection was controlled by a Dantec PIV2100 processor. Polyamid particles with a mean diameter of 20 μm were used as seeding. The Kodak Megaplus ES 1.0 has a resolution of 1008×1016 pixels, with a pixel size of 9 μm, giving a total chip size of approximately 9.1×9.2 mm^2. During the measurements, the camera was placed such that the image covered exactly the object plane. Thus, with a measuring domain of 200×200 mm^2, a magnification factor of M=9.2/200=0.046, based on image height, was used in the measurements. Using the following formula for calculation of the diffraction-limited minimum image diameter (Raffel et al. 1998):

$$d_\mathrm{d} = 2.44 f^{\#}(\mathrm{M}+1)\lambda, \qquad (1)$$

where $f^{\#}$ (the f-number) is the numerical aperture of the camera and λ=532 nm is the wavelength of the laser light, it was found that using $f^{\#}$=11 was appropriate to ensure that a particle image covered 1–2 pixels on the CCD chip, thus minimizing the measurement errors caused by pixel locking (see Westerweel 2000). Having chosen an appropriate f-number, three parameters were optimized in order to obtain high quality recordings:

- image density, N_I,
- time between pulses, Δt,
- time between recordings, t_0.

Following Keane and Adrian (1990), the image density, N_I, should be at least 15 to get a good PIV recording. Further, the in-plane and out-of-plane displacements should not exceed 25% of the interrogation area (IA) side length or the laser-sheet thickness, respectively. An IA size of 32×32 pixels was used for the analysis of the PIV images. Thus, to make sure that the requirement $N_\mathrm{I}\geq 15$ was met, seeding was added to the flow until a zoom of the image maps containing an area of approximately 32×32 pixels showed a density of about 20 particle pairs. The time between pulses was set to Δt=3,500 μs. This yielded an in-plane displacement slightly higher than 25% of the IA side length in the jet region. However, good velocity data in this

region was still obtained by use of *adaptive correlation*. The laser-sheet thickness was approximately 1 mm, corresponding to about 20% of the IA side length. Thus, assuming the out-of-plane displacement to be less than 20% of the in-plane displacements, the requirement of less than 25% out-of-plane displacement was also met. Measurements with LDA were performed in representative points of the domain prior to the PIV measurements. Integrating the autocorrelation function it was found that the integral time scales in the jet region are on the order of 10 ms. In the bottom region of the domain, however, time scales as high as 1.5 s were found. Thus, to make sure that the measurements for use in the statistical analysis were independent, the time between recordings was set to t_0=3 s. A total of 500 images were sampled. The data used for the study of the temporal evolution of the flow were taken at the maximum frequency of the system, namely 10 Hz. The total number of images recorded was 100.

3 Data reduction

In the following, a brief explanation of the processing of the PIV data and a short review on the theory behind the POD is given.

3.1 Image processing

The images were processed with Dantec FlowManager ver. 3.40 (Dantec, Skovlunde, Denmark) using adaptive correlation. Adaptive correlation is especially well suited for flow fields where big differences in mean flow velocities are present. This is the case for the flow in the Annex 20 room, where the velocities in the wall jet region are significantly larger than in the regions away from the jet. The images were processed using one refinement step going from initially 64×64 pixels to the final resolution of 32×32 pixels per IA. After each step, the vector maps were filtered to remove spurious vectors by substituting each vector with the uniformly weighted average of the vectors in a neighborhood of 3×3 vectors. A 25% overlap was used in the processing, yielding vector maps of 41×42 vectors each in total.

3.2 POD

The POD, also known as the Karhunen–Loeve expansion, was first introduced in fluid mechanics by Lumley (1970) and is based on energy considerations. Several versions of the POD have been developed and used since then. In the present analysis, the so-called snapshot method suggested by Sirovich (1987) is applied. The discrete PIV data from each vector map (snapshot) are arranged in vectors, $\mathbf{x}_i$. By subtracting the ensemble average from each realization, vectors, $\mathbf{v}_i$, containing the fluctuating part of all velocities in the domain for the i-th snapshot, are obtained. Thus, with n snapshots:

$$\mathbf{v}_i = \mathbf{x}_i - \frac{1}{n}\sum_{j=1}^{n}\mathbf{x}_j, \; i = 1 \ldots n \tag{2}$$

From these vectors an $n \times n$ autocovariance matrix, $\mathbf{R}$, is formed with elements:

$$R_{ik} = \mathbf{v}_i \cdot \mathbf{v}_k. \tag{3}$$

Solving the algebraic eigenvalue problem for this matrix an orthonormal basis can be constructed as

$$\phi^k = \frac{\sum_{i=1}^{n} g_i^k \mathbf{v}_i}{\left\| \sum_{i=1}^{n} g_i^k \mathbf{v}_i \right\|}, \tag{4}$$

where g_i^k is the i-th component of the normalized eigenvector corresponding to the k-th eigenvalue, λ_k. An eigenvalue represents the total energy contained in the corresponding mode given by Eq. 4. Hence, ordering the eigenvalues as $\lambda_1 > \lambda_2 > \ldots > \lambda_{n-1} > 0$, the first modes found are the most energetic ones. In this way, interpreting a given mode as a coherent structure, the first modes represent the largest, most dominant structures of the flow.

Having constructed the orthonormal basis, the original flow field may be reconstructed by

$$\mathbf{V} = \Phi\mathbf{A}, \tag{5}$$

where Φ, $\mathbf{V}$ and $\mathbf{A}$ are matrices containing the ϕ^k, the $\mathbf{v}_k$ and $\mathbf{a}^k$ vectors columnwise, respectively, the latter being the coefficient vector associated with $\mathbf{v}_k$. With velocity data sampled at a given frequency this can be utilized to determine the coefficients, or amplitudes, $\mathbf{a}$, of the POD modes as a function of time. Since the POD modes form an orthonormal basis, Eq. 5 leads to

$$\mathbf{A} = \Phi^T\mathbf{V}. \tag{6}$$

Knowing the coefficients, $\mathbf{a}^k$, a given snapshot may then be reconstructed as follows:

$$\mathbf{x}_k \approx \sum_{i=1}^{m} \phi^i a_i^k + \frac{1}{n}\sum_{j=1}^{n}\mathbf{x}_j. \tag{7}$$

The value of m specifies the number of basis modes included in the reconstruction. The number of modes needed to get a satisfactory representation depends on the complexity of the flow. What is of interest in the present case, however, is the behavior of the amplitudes, $\mathbf{a}$. Investigation of the temporal evolution of $\mathbf{a}$ yields a picture of how the influence of the different POD modes varies in time.

4 Results and discussion

4.1 Vector maps and flow statistics

Figure 3 shows the ensemble average of the 500 independent instantaneous vector maps and the contours of the turbulent kinetic energy estimated as $(\overline{u'u'} + \overline{v'v'})$ normed with u_0^2. The mean field velocities have been scaled by a factor of 0.1 to yield suitable vector lengths. Using this scaling, the mean inlet velocity, u_0, corresponds to 45 mm or just below one-fourth of the domain width. The flow is divided into a high-velocity wall jet in a thin region at the upper boundary and a large low-velocity region below the

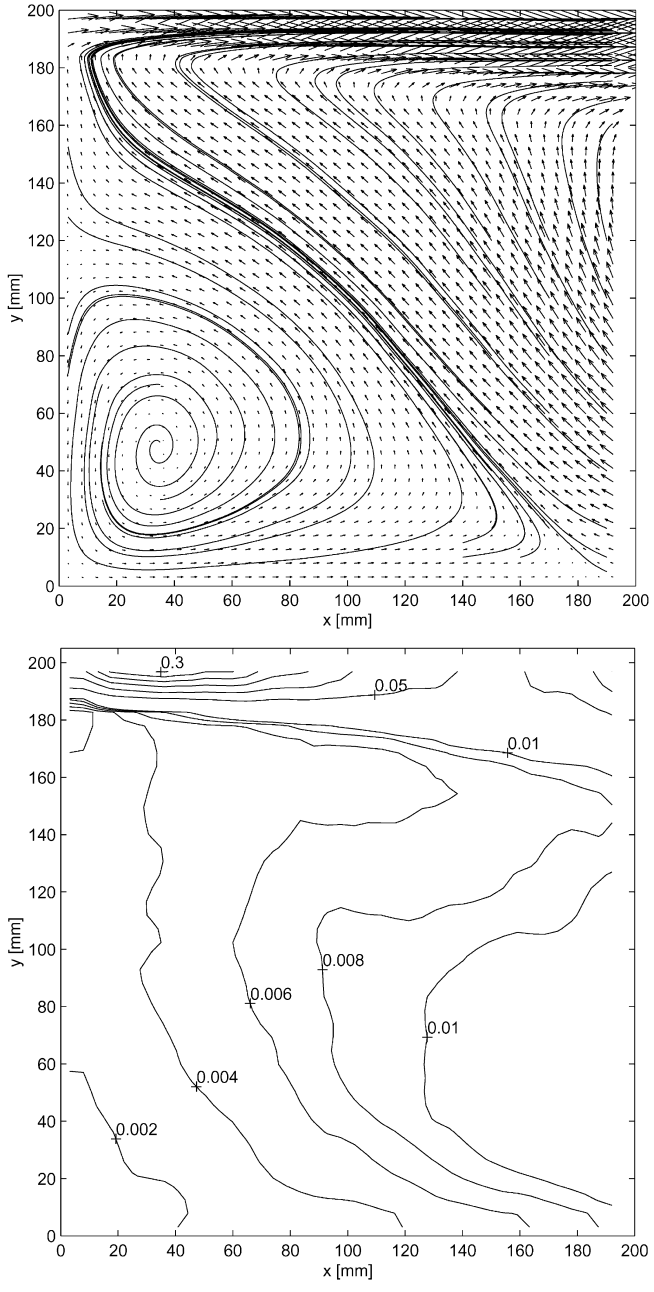

Fig. 3. *Top*: ensemble average with sectional streamlines of 500 instantaneous vector maps. *Bottom*: distribution of turbulent kinetic energy given by $(\overline{u'u'} + \overline{v'v'})/u_0^2$)

wall jet. The velocities in the low-velocity region are on the order of 5% of u_0.

Sectional streamlines have been added to the mean flow vector map. The streamlines clearly reveal the characteristic recirculation zone, which appears at the lower left corner of the Annex 20 room. The size of the recirculation zone is well defined by the singular points on the left and bottom walls at $y \approx 110$ mm and $x \approx 180$ mm. It should be noted that this is a significantly larger recirculation zone than indicated by recent results from numerical simulations with RANS employing the k–ϵ model (Voigt 2001). Qualitatively, however, the present results and the simulations in Voigt (2001) are in good agreement.

The contours of the estimate of turbulent kinetic energy show that the highest turbulence levels are found in the regions with the highest mean velocities. The levels of the turbulent kinetic energy in the low-velocity region are in the order of 2% of the levels found in the wall jet. Thus, the velocity fluctuations are a factor of seven smaller in this region than in the jet region. In the low-velocity region, the velocity fluctuations are therefore larger than the local mean velocities. This indicates that other flow structures than the ones found in the mean velocity field are important for the flow in this region.

Figure 4 shows two examples of instantaneous vector maps (snapshots). Here also, the velocities have been scaled by a factor of 0.1. The first snapshot has a flow field similar to the mean velocity field shown in Fig. 3 with a general movement from the lower right directed towards

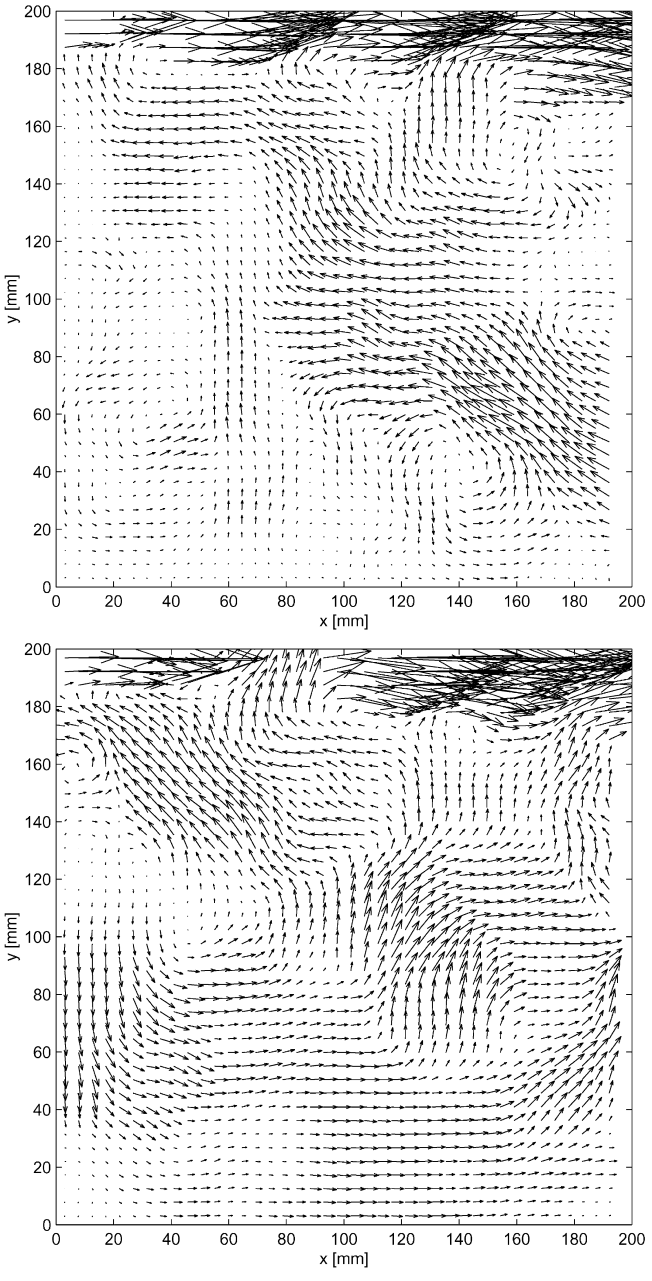

Fig. 4. Examples of instantaneous vector maps

the inlet. This is the case for many of the snapshots. However, a significant part of the snapshots show flow structures very different from the mean velocity field. An example is the second snapshot shown in Fig. 4. Here, several small regions with different flow directions are present. In both examples, the wall jet region seems to consist of 'bursts' of small regions with high velocities. These bursts are seen in the majority of the snapshots and typically cover x intervals of about 0.2–0.4 H.

It might be suspected that the bursts observed in the jet region are a result of the experimental conditions (pump, etc.) rather than an actual feature of the flow in the domain considered. To check the inlet conditions, LDA measurements were performed in the center of the jet region 50 mm up- and downstream of the inlet. The frequency spectra did not reveal any peaks indicating a periodic variation in the inlet conditions. This supported the assumption that the bursts observed in the PIV data are indeed a characteristic feature of the flow in the Annex 20 room, and not just an artifact of the experimental setup.

4.2
Dominant structures

The POD technique has been applied to extract the dominant structures of the flow in the measuring domain. Figure 5 shows the relative energy of POD modes 1–20 compared to the total energy of the data set. The first 20 modes capture approximately 71% of the total energy. The curve decays rapidly in the beginning, but becomes less and less steep the higher the mode number. The lower energy levels indicate smaller flow structures, or equivalently, more detailed information about the flow. The first, most energetic modes represent the dominant, large structures of the flow. For instance, it can be seen from Fig. 5 that mode 1 alone contains more than 12% of the total energy.

A selection of POD modes is shown in Fig. 6 (the vectors have been scaled by a factor of 0.2). The first 10 modes can roughly be divided in modes related to the wall jet and modes related to the large-scale flow structures in the low-velocity region. Modes 1, 3, 4, and 8 have large vectors in the wall jet region compared to the low-velocity region, while modes 2, 5, 6, 7, 9, and 10 have similar vector lengths all over the domain. This suggests that the dynamics of the wall jet region and the low-velocity region are different. Modes 1 and 2 both have similar flow structures with a single 'burst' of large vectors in the positive x direction appearing in the wall jet region. The burst in mode 1 is situated at $x/H \approx 0.2$ and the low-velocity region vectors are in the opposite direction of the mean flow velocities. In mode 2, the burst is very close to the inlet and there is a strong flow into the domain at the lower part of the right boundary. Both modes therefore show a correlation between a velocity burst at the inlet and an inflow/outflow in the lower right part of the domain.

Modes 3 and 4 have vectors in negative x direction at the inlet and a region of long vectors in the downstream part of the wall jet region. Mode 3 has a burst at $x/H \approx 0.3$ and mode 4 has a negative burst at $x/h \approx 0.8$. Thus, modes 3 and 4 relate to the dynamics of bursts in the downstream part of the wall jet. Modes 5 and 7 both consist of a single large vortex in the low-velocity region. This flow structure is completely different from the mean velocity field. Modes 5 and 7 also have significant vectors in the downstream part of the wall jet region, but in opposite directions. Mode 6 contains a part of a vortex with opposite sign of the one in modes 5 and 7, but also has a burst at the downstream part of the wall jet region. All in all, these three modes suggest that there is some correlation between the large vortex structure and the dynamics of the downstream part of the wall jet region. Mode 9 has a large inflow at the upper part of the right boundary and a smaller outflow at

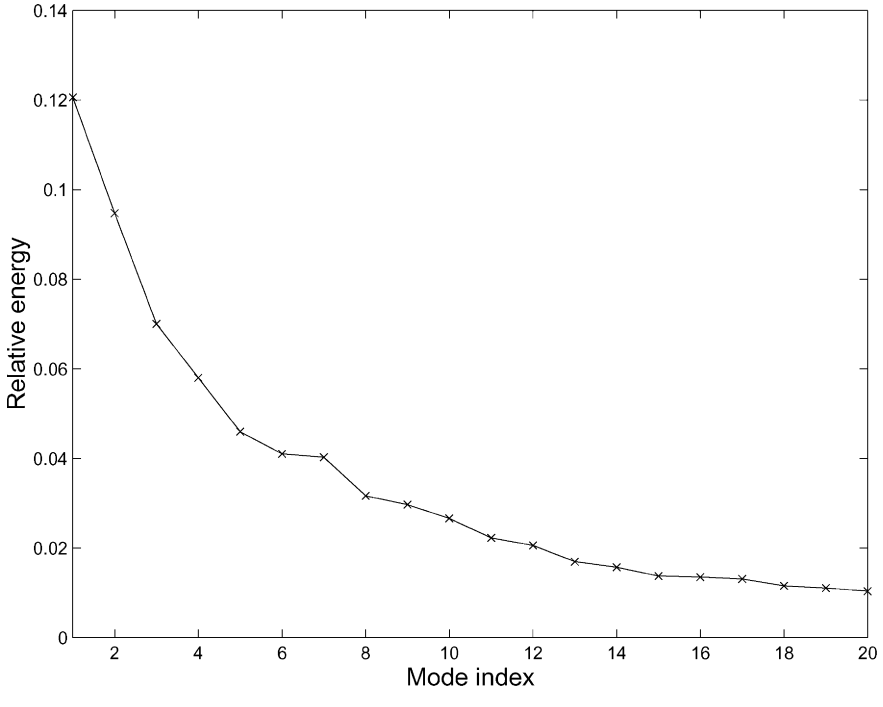

Fig. 5. Relative energy of first 20 POD modes

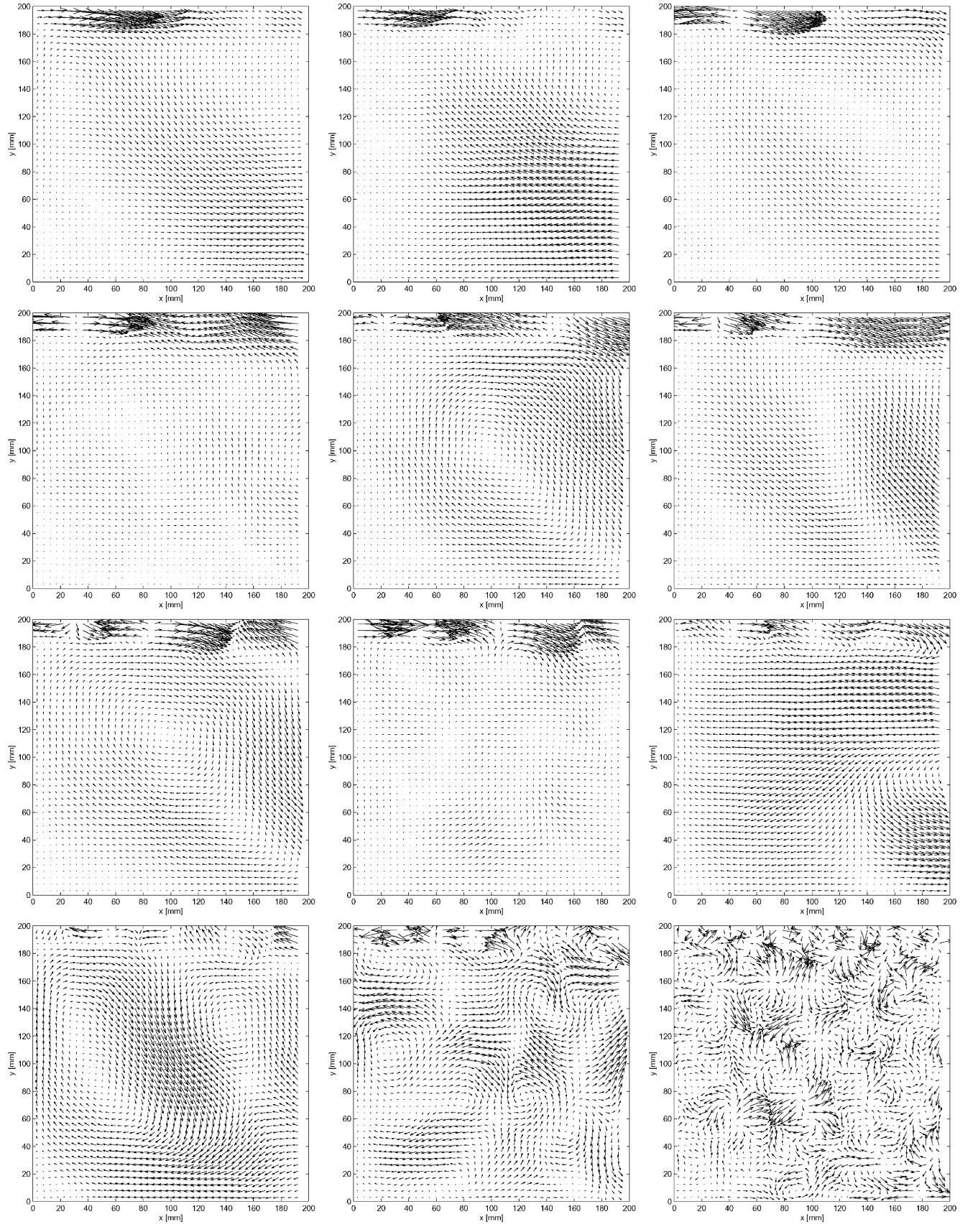

Fig. 6. From left to right: POD modes 1–10, 50, and 200

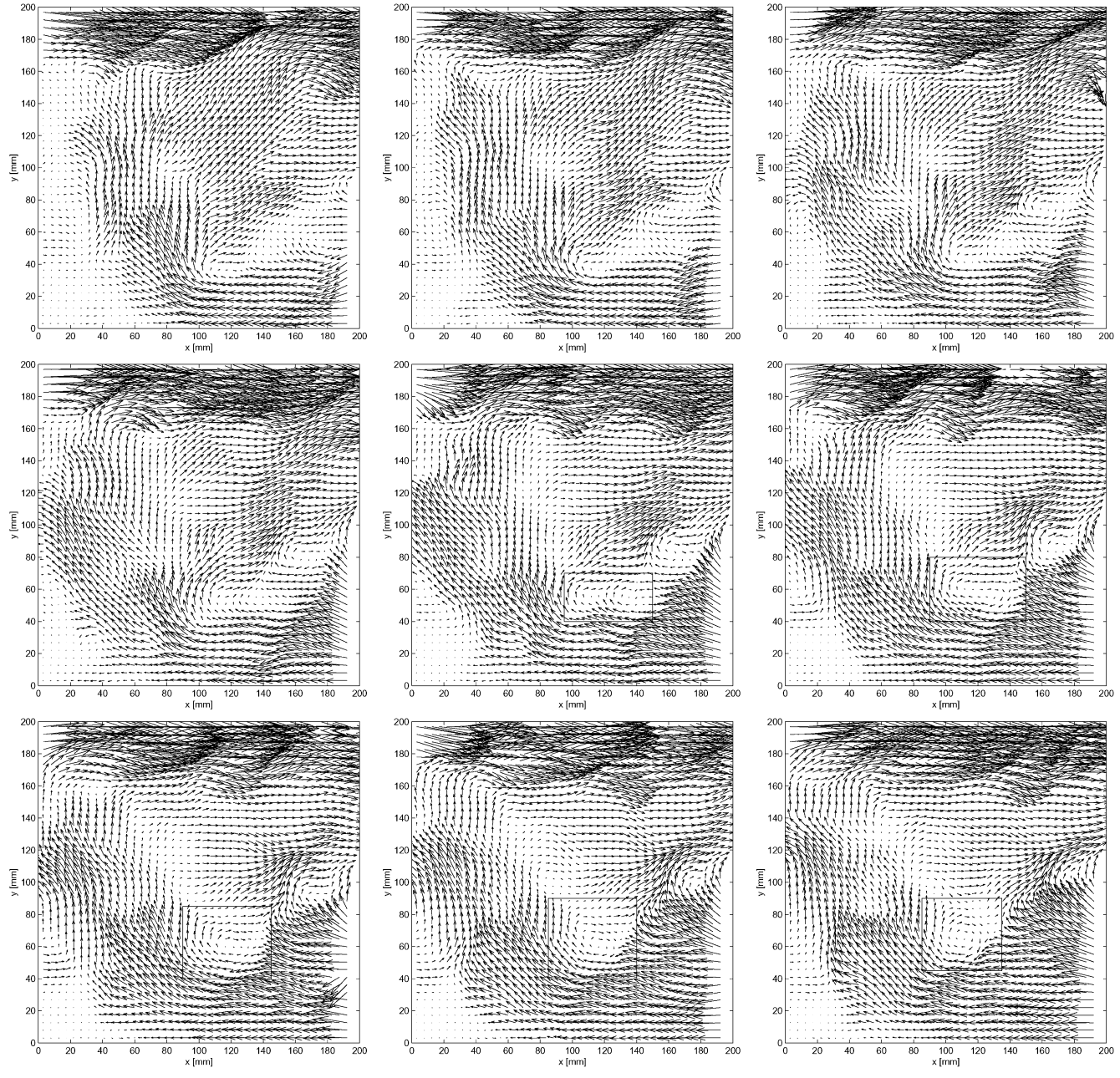

Fig. 7. From left to right: sequence of snapshots taken at 10 Hz. The merging of two small vortices into one is marked with a *rectangle*

the lower part of the same boundary. A complex flow pattern is found in POD mode 10. Compared to the other modes related to the low-velocity region, this mode offers a greater level of detail. It consists of three vortices and a separation point. Two of the vortices are situated on the left side of the domain and the third one, which appears in connection with the separation point, on the right. Like modes 2, 5, 6, and 7, modes 9 and 10 are connected to the dynamics of the low-velocity region, but are now representing flow structure at a lower energy level.

To elaborate on the behavior of the POD modes with decreasing energy level, the last two pictures show POD modes 50 and 200. Considering the first 10 POD modes in Fig. 6, it seems that the level of detail increases with the mode number. Modes 1 and 2, which together capture 21.6% of the total energy, consist of large regions with uniform velocities, while mode 10, which represents 2.7% of the total energy, contains information about the presence of vortices and separation points in the low-velocity region. Mode number 50 represents only 0.3% of the total energy, but shows a very high level of detail, with several small vortices scattered over the domain. This is in agreement with the theoretical description of the POD and the general observation that the lower the energy level, the more flow detail is offered in a given POD mode. However, depending on how many snapshots are included in the analysis, there may be an upper limit of mode number to which it makes sense to talk about flow structures in the modes. The last POD mode shown, number 200, is an example of this. This mode contains information about

small-scale motion only and as such cannot be interpreted as representative of flow structure.

4.3 Temporal evolution

The study of the temporal evolution of the flow is based on 100 images taken at 10 Hz. Several snapshots of each flow structure are obtained with this time resolution. A sequence from the series consisting of nine successive snapshots (0.8 s) is shown in Fig. 7. The vectors have been scaled by a factor of 0.1 as in Figs. 3 and 4. Evidently, the velocities for this particular sequence are larger than on average and the wall jet region is somewhat wider than normal. As explained below, the general structure of the flow field involves a large inflow at the bottom part of the domain, which is probably the cause of the enhanced jet flow, simply due to continuity.

The overall structure of the sequence is uniform jet motion in the positive x direction balanced by a large region with vectors pointing in the negative x direction in the bottom of the domain and a small region to the lower left with zero velocities. In the rest of the domain, the flow changes throughout the sequence. One example is the merging of two small vortices into one, which occurs in the neighborhood of $(x,y)\approx(120,50)$ mm. The process is marked with rectangles in Fig. 7. This example shows how small-scale changes may be followed directly from the PIV data in the low-velocity region.

The 100 snapshots taken at 10 Hz were not included in the POD analysis. However, by projecting the fluctuating part of the velocity fields onto the POD basis, the amplitudes, a_i, representing the relative influences of the different modes in a given snapshot, may still be obtained. Figure 8 shows the POD amplitudes of the first 10 modes as functions of time for the 100 snapshots taken at 10 Hz. The amplitudes of mode 1, 3, 4, and 8 are relatively small and have rapid fluctuations. As discussed earlier, these modes are related to the dynamics of the wall jet. The amplitudes of mode 2, 5, 6, 7, 9, and 10, which were found to be related to the dynamics of the low-velocity region, are generally larger and have slower variations. Evidently, there are two different time scales for the two regions. In fact, the time scale of the dominant structures in the low-velocity region seems to be longer than the 1.5 s found from the autocorrelation of an LDA signal in a single point (cf. Sect. 2).

The two vertical lines imposed on the plots indicate the start and ending point of the sequence shown in Fig. 7. As mentioned above, the large-scale motion of the flow sequence shown in Fig. 7 is characterized by a movement in positive x direction in the upper part of the domain, negative x direction in the lower part, and a small region to the lower left with vanishing velocities. This overall flow pattern is reflected in the amplitudes of the POD modes. The coefficients of modes 5, 7, and 10 are all large and positive throughout the interval considered. Combining this with the flow structures represented in the first 10 modes of Fig. 6 reveals that the contributions from these three modes act to cause this overall flow pattern. Further, the amplitude of mode 9 is large and negative, which is connected to the region of vectors just below the jet region to the right, all pointing in the positive x direction.

Another interesting interaction between a number of the first modes is discovered by looking at the coefficients a_1, a_2, and a_6. In the beginning of the sequence, the amplitude of mode 1 is large and positive, the amplitude of mode 2 close to zero, and the amplitude of mode 6 is large and negative. During the 0.8 s of the time sequence, a_1 and a_6 decrease towards zero, while the coefficient of mode 2 grows from zero to a large positive value. The corresponding change in flow pattern is evident in Fig. 7. In the first vector maps, the region slightly below the middle to the right is characterized by very low velocities. With positive and negative coefficients, respectively, modes 1 and 6 both act in the opposite direction of the mean flow in this area. With a_1 and a_6 decreasing towards zero and a_2 growing to a large positive value, the situation is changed. A large uniform region with velocities directed towards the center of the domain emerges to the lower right, clearly showing the dominance of POD mode 2 in the last snapshots of the sequence.

The present example is a specific case of the behavior of a few of the POD coefficients related to a change in the corresponding flow pattern. It was found that the overall flow pattern for the time sequence considered was dominated by POD modes 5, 7, and 10 apart from the mean flow field. In general, the large-scale motions of a particular flow are determined by the mean field and a number of the first few POD modes. For simple flows, the large-scale deviations from the mean flow field may be governed by just a few modes, while complex flows like the flow in the Annex 20 room require a larger number. Due to the limited amount of energy contained in the small-scale motions, these are not captured until very high mode numbers (cf. mode 50 in Fig. 6). Thus, while the first few modes determine the large-scale motions, the small-scale structures, such as the vortices marked in Fig. 7, appear as a combination of contributions from the higher order modes.

5 Conclusions

Velocity data has been obtained with PIV in a domain covering a square region near the inlet of a scale model of the Annex 20 room. The flow near the inlet of the Annex 20 room can be divided in two flow regions: the high-velocity wall jet region at the top boundary and the low-velocity region in the domain below the wall jet. The latter is of special interest because this is where persons will be influenced by the air movements. In the low-velocity region, the velocity fluctuations are larger than the mean velocities. The reason for this is that the low-velocity region sometimes has flow patterns very different from the mean flow.

POD analysis offers new insight into the flow structures. The first 10 POD modes can roughly be divided into modes mainly related to the wall jet and modes that relate to the complete domain. The first two modes (which contain most energy) have horizontal in- or outflow at the lower part of the right boundary of the domain. This shows that fluid often enters (and sometimes leaves) the low-velocity region in 'bursts' of nearly horizontal velocity. This is in contrast with the mean velocity field, where fluid

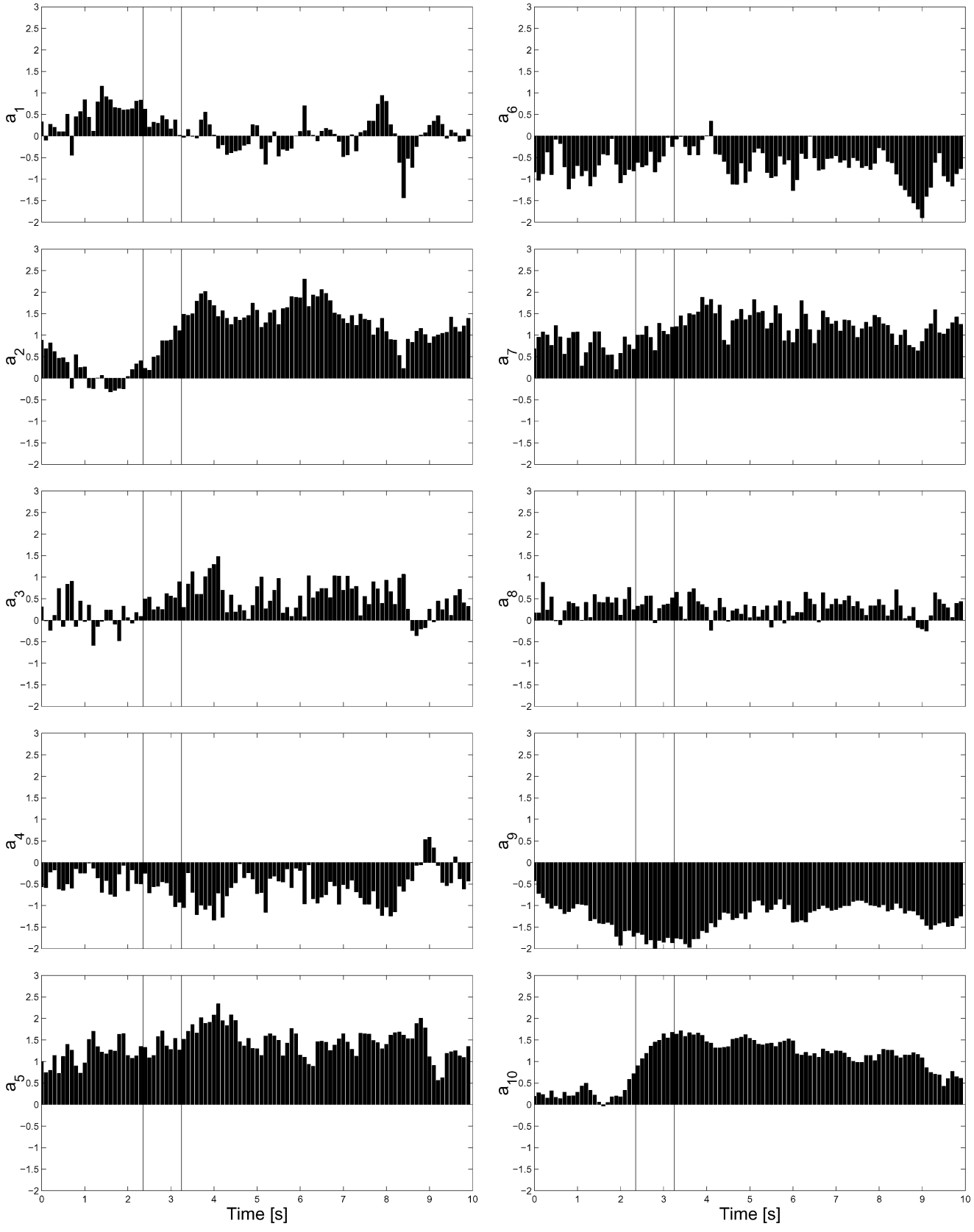

Fig. 8. Time history of amplitudes of first 10 POD modes. *Vertical lines* mark the time interval of the snapshots shown in Fig. 7

enters at an angle of about 45 degrees to the boundary. The next modes representing flow structure in the low-velocity region are modes 5–7, which all more or less show a single large vortex centered in the middle of the domain. This flow pattern is very different from the mean velocity field, but is often seen in the complete series of snapshots from the measurements.

The wall jet region contains 'bursts' of small regions with high velocities, which normally cover x intervals of about 20–40% of the domain width. These bursts are seen at different positions in all the first eight POD modes. In the first two modes, the bursts are situated near the inlet. This indicates that there is a connection between the appearance of the burst and an inflow (positive or negative) into the domain near the bottom wall. The bursts could be related to three-dimensional flow structures in the wall jet and to the pressure fluctuations in the room. A more thorough investigation of this would require measurements in the z direction and probably longer time series.

The investigation of the POD mode coefficients for a time series show that there are two different time scales in the flow: a rapid time scale related to the wall jet and a slow time scale related to flow structures in the low-velocity region. It is interesting to note that the slow time scale can be of many seconds. This is significantly longer than the integral time scale of 1.5 s found by integration of the autocorrelation of an LDA signal in a single point. This stresses the fact that the flow structures have their own dynamics and that they cannot be explained alone by the flow being turbulent. A problem is that the long time scales indicate that a longer time between recordings would possibly yield statistically more accurate results of the POD analysis.

A traditional CFD simulation using Reynolds-averaged Navier–Stokes equations and a turbulence model like the k–ϵ model has difficulty in predicting the actual flow in the room. However, even a perfect Reynolds-averaged calculation yielding the result presented in Fig. 3 would not represent the actual flow very well. For human comfort, parameters like draught (maximum local velocities) and transport of pollutants are important. To estimate such factors correctly by calculations, it is necessary to make time-dependent simulations. This makes LES an obvious choice. Results from LES calculations could then be compared to the present measurements, for example, by comparison of the results of a POD analysis.

References

Chen Q (1995) Comparison of different k–ϵ models for indoor airflow computations. Numer Heat Transfer B 28:353–369

George WK, Abrahamsson H, Eriksson J, Karlsson RI, Löfdahl L, Wosnik M (2000) A similarity theory for the turbulent plane wall jet without external stream. J Fluid Mech 425:367–411

Keane RD, Adrian RJ (1990) Optimization of particle image velocimeters. Part I: double-pulsed systems. Meas Sci Technol 1:1202–1215

Lumley JL (1970) Stochastic tools in turbulence. Academic Press, London

Moin P, Moser RD (1989) Characteristic-eddy decomposition of turbulence in a channel. J Fluid Mech 200:471–509

Nielsen PV (1990) Specification of a two-dimensional test case. International Energy Agency, Annex 20: air flow pattern within buildings. R9040. Department of Building Technology and Structural Engineering, Aalborg University, Denmark

Nielsen PV, Restivo A, Whitelaw JH (1978) The velocity characteristics of ventilated rooms. Fluids Eng 100:291–298

Raffel M, Willert C, Kompenhans J (1998) Particle image velocimetry – a practical guide. Springer, Berlin Heidelberg New York

Sirovich L (1987) Turbulence and the dynamics of coherent structures. Part 1: coherent structures. Q Appl Math 45:561–571

Voigt LK (2001) Navier–Stokes simulations of airflow in rooms and around a human body. PhD dissertation. Department of Mechanical Engineering, Technical University of Denmark, Lyngby, Denmark

Westerweel J (2000) Effect of sensor geometry on the performance of PIV interrogation. In: Adrian RJ, Durao DFG, Durst F, Heitor MV, Maeda M, Whitelaw JH (eds) Laser techniques applied to fluid mechanics. Springer, Berlin Heidelberg New York, pp 37–56